Science Advances

AAAS

advances.sciencemag.org/cgi/content/full/2/11/e1600974/DC1

Supplementary Materials for

Uncovering the forces between nucleosomes using DNA origami

Jonas J. Funke, Philip Ketterer, Corinna Lieleg, Sarah Schunter, Philipp Korber, Hendrik Dietz

Published 23 November 2016, *Sci. Adv.* **2**, e1600974 (2016)
DOI: 10.1126/sciadv.1600974

This PDF file includes:

- fig. S12. Exemplary particles of the force spectrometer with two bound NCPs (wild-type and *X. laevis*) at the distal position.
- fig. S13. Average micrographs of force spectrometers with attached NCPs (wild-type and *X. laevis*) at the proximal position.
- fig. S14. Negative staining versus cryo-EM micrographs.
- fig. S15. Comparison of single particles from negative staining versus cryo-EM.
- fig. S16. Quantitative comparison of distributions and energy landscapes from negative staining versus cryo-EM.
- fig. S17. Calculation of FRET efficiencies and depiction of laser-scanned agarose gels.
- fig. S18. Nucleosome-nucleosome interaction observed using gel-based ensemble FRET measurements.
- fig. S19. Gel-based ensemble FRET measurements of nucleosome variants and orientations.
- fig. S20. Calculation of free-energy landscapes.
- fig. S21. Configuration of nucleosomes on the force spectrometer.
- fig. S22. Gay-Berne potential fits.

note S1. Reconstitution of nucleosomes with single-strand branches

Salt gradient dialysis reconstitution of nucleosomes was done as described (34) but BSA and IGEPAL were omitted from the reconstitution buffer as they interfere with TEM imaging. We used either *Drosophila* embryo (52) or recombinant *Xenopus laevis* (purchased from the Protein Expression/Purification Facility at Colorado State University) histones. *Drosophila* embryo histones contain some modifications (53), while the recombinant histones allow studying modification-free or specifically modified/truncated histones. Different species as histone source can be used in our studies as the sequences of rodent, chicken, human, fly (*D. melanogaster*) and frog (*X. laevis*) histones are nearly identical (54). Recombinant *Xenopus* histones were either wild type or tail-less, with the latter encompassing only the trypsin-resistant globular domains as described (55), or were acetylated by MOF acetyltransferase (see below), which is largely specific for lysine 16 of histone H4 (38). The branched DNA templates were based on 147 bp of the Widom 601 nucleosome positioning sequence (33) to obtain strong and homogeneous positioning and had 20 nt single strand branches (see below). We validated that such nicked and branched templates became reconstituted by gel electrophoresis and negative-staining TEM. Nucleosomes with up to four nicks and single strand branches were analyzed by native gel electrophoresis alongside with nucleosomes reconstituted onto continuously double stranded 147 bp templates (Fig. 2b). Nucleosomes were more retarded with single strand branches (Fig. 2b, lanes 6,8 versus 2,4) or without histone tails (fig. S1b, lanes 4,5 versus 2,3). The absence of free DNA (fig. S1b) confirmed complete reconstitution, and SDS-PAGE confirmed stoichiometric incorporation of all four histones (fig. S1c). Nucleosomes with nicked versus continuous DNA showed similar stability in the presence of increasing salt concentration, i.e. both were equally stable at up to 600 mM NaCl and the major fraction of nucleosomes was dissociated between 1.2 and 1.4 M NaCl (fig. S2, a and b), which is in good agreement with the stability for 601 nucleosomes at up to 1.26 M monovalent salt (35). Our reconstituted NCPs remained stable under high Mg^{2+} conditions (fig. S2c) that are required for the integrity of DNA origamis. Altogether, this argues that we reconstituted stable nucleosomes suitable to study nucleosome-nucleosome interactions with the force spectrometer. Of note, we reconstituted nucleosome core particles (NCPs) as our constructs lack linker DNA, but we refer in the main article to our NCPs as nucleosomes. The absence of linker DNA as well as linker histones is a prerequisite to study the isolated NCP-NCP interactions.

note S2. Design and assembly of the force spectrometer

One strand of the Widom 601 sequence was divided into six sequences such that the attachment handles protrude radially from the NCP in 90° steps. The sequences are:

Sequence
ATCGAGAATCCCGGTGCCGAGGCCG
(A1)-CTCAATTGGTCGTAGACAGC
(A2)-TCTAGCACCGCTTAAACGCAC
(A3)-GTACGCGCTGTCCCCCGCGT
(A4)-TTTAACCGCCAAGGGGATTACTCCCTAGTCTC
CAGGCACGTGTCAGATATATACATCCGAT

The single stranded attachment handles were always placed at the 5'-end of the respective strand. The sequences used for the attachments handles were designed with NUPACK (51):

Handle	Sequence set 1 (bottom beam)	Sequence set 2 (top beam)
A1	AACTCGTCTGTTGGTGGCGG	AGTGTGACACACCTGCGGGC
A2	CTCCTCCTCCTCCCGCAGGT	GCAGAACGTTGAAGAAGTTG
A3	GCCGCAGGATACAGAATACG	CGTAGAGTACGCATAAATAT
A4	TCCTCAGACTTAACACAGGG	AGATCTTCTAGCGGAGGATA

Sequences are summarized in fig. S3.

Preparation of branched template DNA

For reconstitution of NCPs with continuous dsDNA, 147bp dsDNA fragments based on the 601 sequence (4) were produced by PCR amplification (primers: 5'- ATCGAGAATC CCGGTGCCGAG-3' and 5'-ATCGGATGTATATATCTGACACGTGCCTG-3'; DNA template: 601 sequence cloned via A-overhangs within TOPO-TA pCR 4.0 vector (Invitrogen)). For NCPs with nicked or nicked and branched templates, the templates for reconstitution were generated by hybridization of respective oligonucleotides to a continuous 147 nt single DNA strand, which was synthesized by Integrated DNA Technologies (IDT), Leuven, Belgium and PAGE purified. All other oligonucleotides were synthesized in HPSF grade by Eurofins Genomics, Ebersberg, Germany. Hybridization of the oligonucleotides was by heating to 60°C and cooling to 40°C in steps of 1°C/h in 10 mM Tris-HCL, pH 7.6, 2 M NaCl and 1 mM EDTA. Complete annealing of all oligonucleotides to dsDNA was confirmed by agarose gel electrophoresis prior to nucleosome reconstitution.

Histone Acetyltransferase Assay with MOF

Recombinant Flag-tagged MOF histone acetyltransferase was expressed via the Baculovirus expression system (Thermo Fisher) in Sf21 cells using pFastBac1 encoding Flag-tagged MOF and purified by FLAG affinity chromatography as described (56). Histone H4 acetylation by recombinant MOF was confirmed using 0.25 µCi [^{3}H]-acetyl-CoA (60 pmol, Hartmann Analytik), 400 ng recombinant WT *Xenopus* histone octamers, and 150 ng or 600 ng MOF in 20 µl. Histone acetylation was monitored by filter binding and fluorography (38). Briefly, acetylation reactions were incubated for 30 min at 26°C, spotted onto p81 filters (Schubert & Weiss), washed three times with 50 mM sodium carbonate (pH 9.3) at room temperature and filters were counted in a scintillation counter (Beckman LS1801, scintillation cocktail Ultima Gold, Perkin Elmer). Incorporated counts were the same for both MOF concentrations. For fluorography, the reactions were stopped with SDS loading buffer and proteins were resolved by SDS-PAGE (4-20% gradient gel, SERVA). The gel was stained with Coomassie blue, treated with AmplifyTM solution (VWR) and exposed to X-ray films (Fuji Super RX). Acetylation of histone H4 was the predominant product as mainly labeled histone H4 and only a minor signal from histone H3 was detected via fluorography (fig. S1a). For large scale preparation, the acetylation reaction was scaled up for 20 µg of histones and 3 µM unlabeled acetyl-CoA (Sigma) and acetylated histones were concentrated (Centricon, MWCO 3kDa, Millipore).

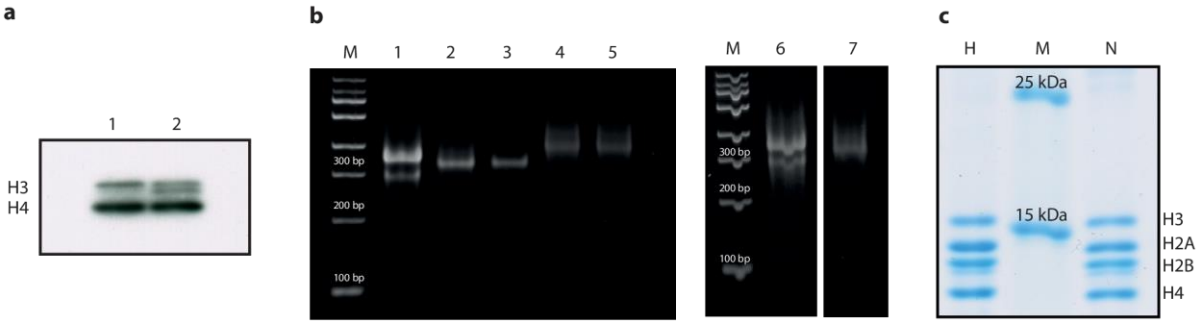

fig. S1. Assembly of wild-type, tailless, and acetylated NCPs with single-strand branches. (**a**) MOF predominantly acetylates histone tails on H4. Histone acetylation was visualized by fluorography of gels after SDS-PAGE (4-20% polyacrylamide gradient gel, SERVA) of recombinant *Xenopus* histones treated with [^{3}H]acetyl-coenzyme A and 1.5 pM (lane 1) or 6 pM (lane 2) MOF. (**b**) To control after salt gradient dialysis the saturation of DNA templates with recombinant *Xenopus* histone octamers (wild type (lanes 2,3), tail-less (lanes 4,5) or acetylated histones (lane 7), respectively), reconstituted NCPs with two single strand branches (A1-A3) were separated on a 4.5% polyacrylamide gel in 100 mM Tris, 83 mM borate, 0.1 mM EDTA at 100 V and 4 °C in parallel with the corresponding free DNA templates (lanes 1,6) followed by ethidium bromide staining. Lane 6 and lane 7 belong to the same gel. M: DNA marker (2-log, NEB). Linear level adjustment was applied to the entire image using Adobe Photoshop CS6. (**c)** To show stoichiometric histone incorporation, NCPs reconstituted with DNA templates with two single strand branches (A1-A3) and *Drosophila* histones (lane N) were precipitated with 10 mM $MgCl_2$ for 10 min on ice to remove unincorporated histones. After centrifugation (10 min, full speed table top centrifuge), precipitated NCPs were resuspended in 10 mM Tris-HCl, pH 7.6, 50 mM NaCl, 1 mM EDTA, separated by SDS-PAGE (17.5% polyacrylamide) in parallel with input *Drosophila* histone octamers (lane H) and a protein size marker (lane M, PeqGold protein marker IV), and Coomassie stained (Colloidal Blue staining kit, Invitrogen). Stained gels were scanned (Epson Perfection V700 scanner) and scan images analyzed using Aida software (Raytest, version 4.27).

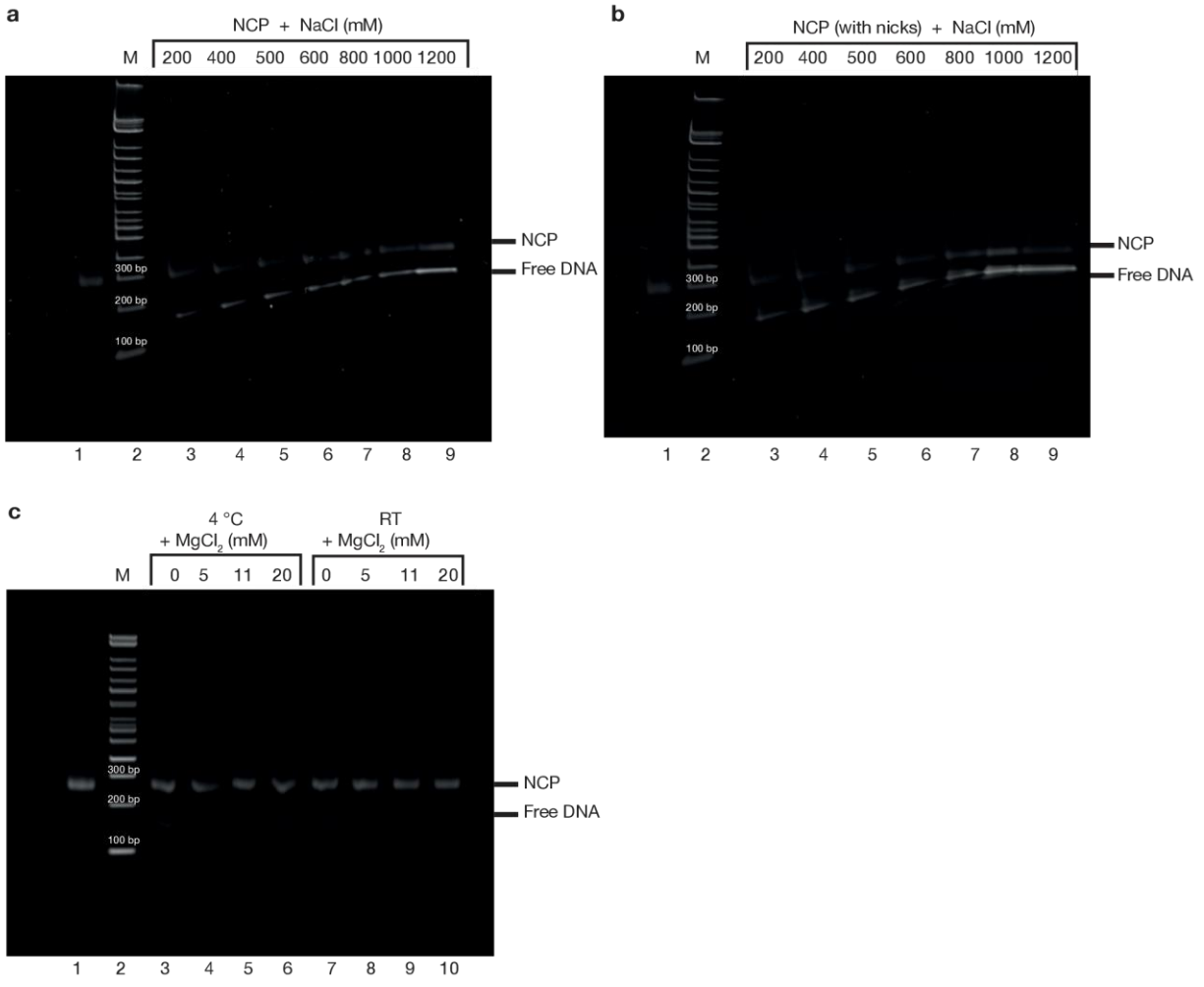

fig. S2. Salt stability of NCPs without or with nicks. (**a**) NCPs reconstituted with *Drosophila* histone octamers on continuous 147 bp 601 templates were incubated for 1 h at 4 °C and the indicated increasing NaCl concentrations (lanes 3-9) and analyzed by native PAGE (4.5% polyacrylamide) followed by ethidium bromide staining; M: DNA marker (2-log, NEB); Lane 1: NCPs without additional NaCl. (**b**) as in a) but with NCPs harboring four nicks at positions described in fig. S3; (**c**), as b) but reconstituted NCPs were incubated for 3 days in the presence of indicated $MgCl_2$ concentrations either at 4 °C (lanes 3-6) or at room temperature (RT, lanes 7-10) in 10 mM Tris-HCl, pH 7.6, 50 mM NaCl, 1 mM EDTA (= no $MgCl_2$) or in 5 mM Tris pH 7.5, 5 mM NaCl, 1 mM EDTA with 5, 11, or 20 mM $MgCl_2$ prior to analysis by native PAGE as in a). Lane 1: NCPs without additional $MgCl_2$ and without 3 days incubation. Gel image manipulation using Adobe Photoshop CS6, if any, involved only linear level adjustments evenly applied to the entire image.

A

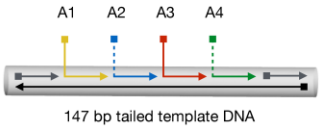

Divided Widom 601 sequence
ATCGAGAATCCCGGTGCCGAGGCCG
(A1)-CTCAATTGGTCGTAGACAGC
(A2)-TCTAGCACCGCTTAAACGCAC
(A3)-GTACGCGCTGTCCCCCGCGT
(A4)-TTTAACCGCCAAGGGGATTACTCCCTAGTCTC
CAGGCACGTGTCAGATATATACATCCGAT

B

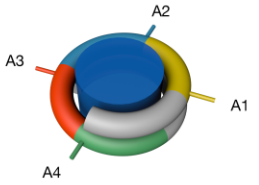

Handle	Sequence set 1 protruding from nucleosome	Sequence set 1 protruding from nucleosome
A1	AACTCGTCTGTTGGTGGCGG	AGTGTGACACACCTGCGGGC
A2	CTCCTCCTCCTCCCGCAGGT	GCAGAACGTTGAAGAAGTTG
A3	GCCGCAGGATACAGAATACG	CGTAGAGTACGCATAAATAT
A4	TCCTCAGACTTAACACAGGG	AGATCTTCTAGCGGAGGATA

C

Sequences protruding from bottom beam of force spectrometer (complementary to set 1)	Sequences protruding from top beam of force spectrometer (complementary to set 2)	Complement to Handle
CCGCCACCAACAGACGAGTT	GCCCGCAGGTGTGTCACACT	A1
CGTATTCTGTATCCTGCGGC	ATATTTATGCGTACTCTACG	A3

fig. S3. Sequences of single-stranded DNA handles protruding from the nucleosome. (**A**) Top: tailed template DNA with up to four single-stranded DNA handles. Bottom: Widom 601 sequence devided into six oligonucleotides with indicated placeholders (A1-A4) for optional ssDNA handles. (**B**) Top: schematic nucleosome with up to four potential ssDNA handles. Bottom: two sets of orthogonal sequences which can protrude at indicated positions (A1-A4) from the nucleosome. (**C**) Set of sequences protruding from the beams of the spectrometer. Due to the advantageous geometry (see fig. S8), only position A1 and A3 were used.

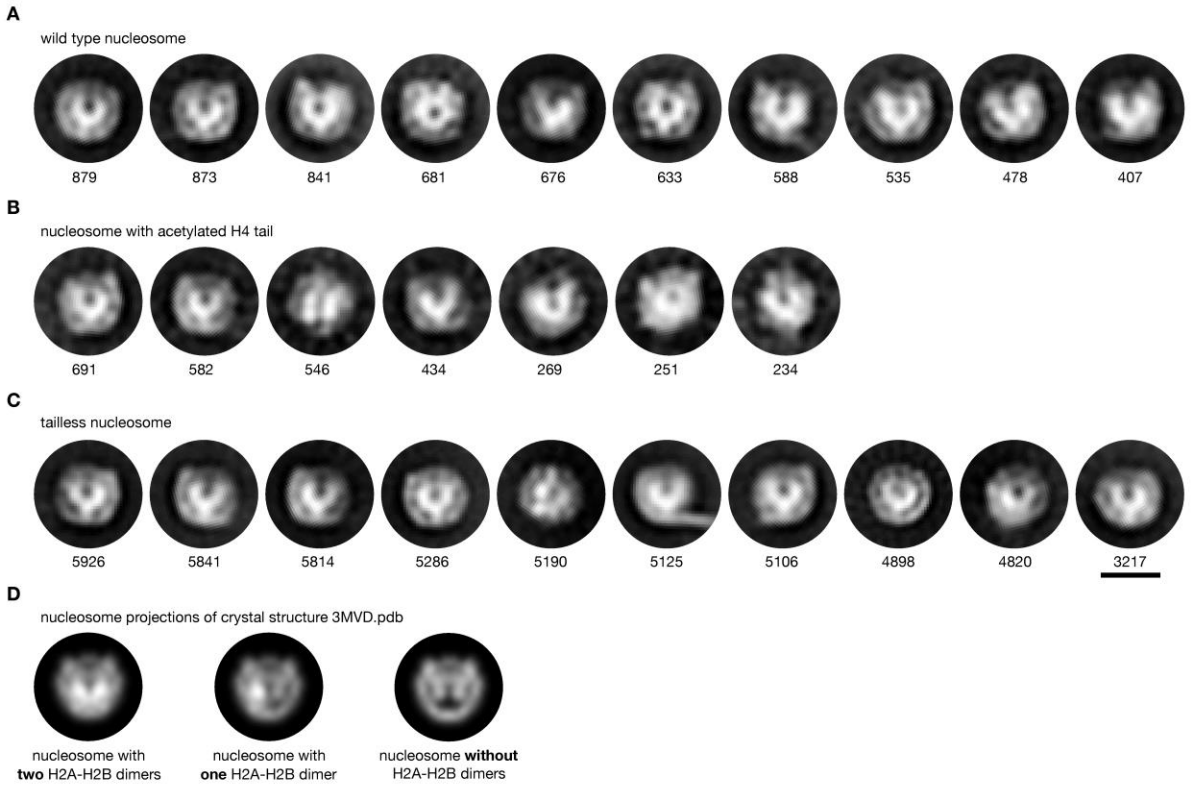

fig. S4. Direct imaging of nucleosomes. Reference-free single-particle electron-microscopy class-averages of negative stained globular wild type nucleosomes (**A**), nucleosomes with acetylated H4 histones (**B**) and nucleosomes without N-terminal tails (**C**). Nucleosomes were reconstituted from *Xenopus laevis* histones. All nucleosomes featured protruding DNA single strands at position A1 and A3. Scale bar: 10 nm. Low-pass filtered (gaussian blur with radius of ~ 0.6 nm) projections of nucleosomes with different stoichiometries of H2A-H2B dimers (**D**) based on the crystal structure 3MVD.pdb.

Design and assembly of the force spectrometer

Design

The force spectrometer is based on the positioner apparatus (32) and was modified using cadnano (57) and CanDo (59). Single-stranded DNA attachment handles for nucleosomes protrude either 15.6 nm (proximal) or 29.6 nm (distal) away from the hinge from the beams of the spectrometer (fig. S5). Two nucleosome handles are separated by approximately 11.4 nm, assuming an effective DNA diameter of 2.2 nm within a DNA origami object.

Self-assembly

The self assembly of the force spectrometer was performed as previously described (58, 32) with reaction mixtures containing 40 nM scaffold DNA (p7704), 200 nM of each DNA oligonucleotide strand, 20 mM $MgCl_2$, 5 mM TRIS base, 1 mM EDTA, 5 mM NaCl (pH ~8). Fluorescently modified DNA oligonucleotides were included in the folding reaction. Oligonucleotides were obtained from Eurofins MWG (Ebersberg, Germany). Reaction mixtures were annealed with a TETRAD (MJ Research, now Biorad) thermal cycling device using an annealing protocol that was optimized according to (60):

Temperature [°]	Duration
65	15 min
58-55	3 h/°
52-50	3 h/°
12	∞

Purification of assembled force spectrometer objects

Assembled force spectrometer objects were purified by means of two rounds of PEG-precipitation (61) and finally dissolved to 160 nM in buffer (11 mM $MgCl_2$, 5 mM TRIS base, 1 mM EDTA, 5 mM NaCl, pH ~8).

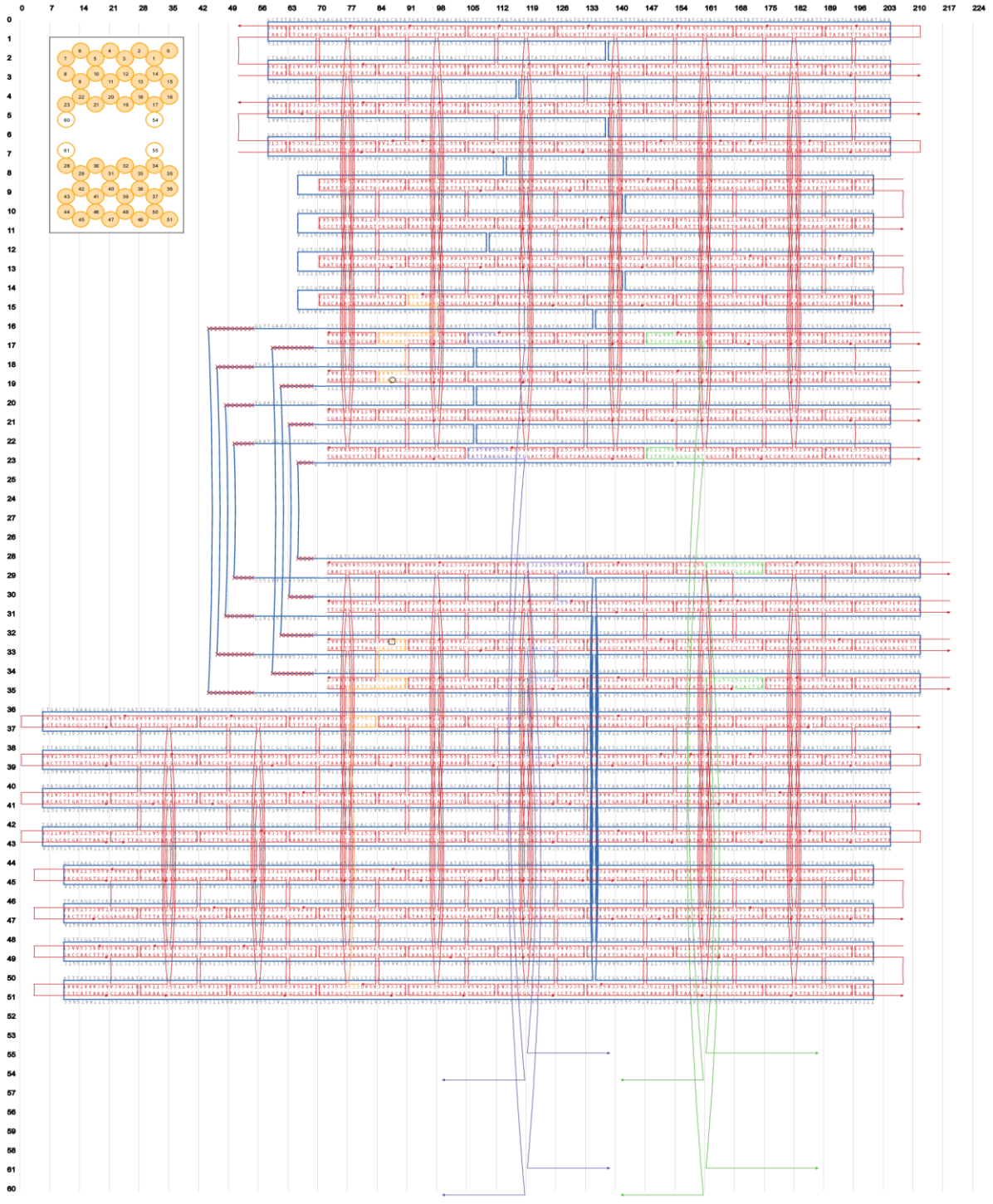

fig. S5. Design diagram of the force spectrometer generated with caDNAno v0.1 (*57*). Oligonucleotides with protruding single-stranded DNA overhangs for the attachment of nucleosomes are colored purple (~47 *bp* away from the hinge) and green (~89 *bp* away from the hinge). Inset: Cross section of the force spectrometer at basepair 77. Black circle: position of base modified with ATTO550 (donor) at the 3'-end. Black circle: position of base modified with ATTO647N (acceptor) at the 3'-end.

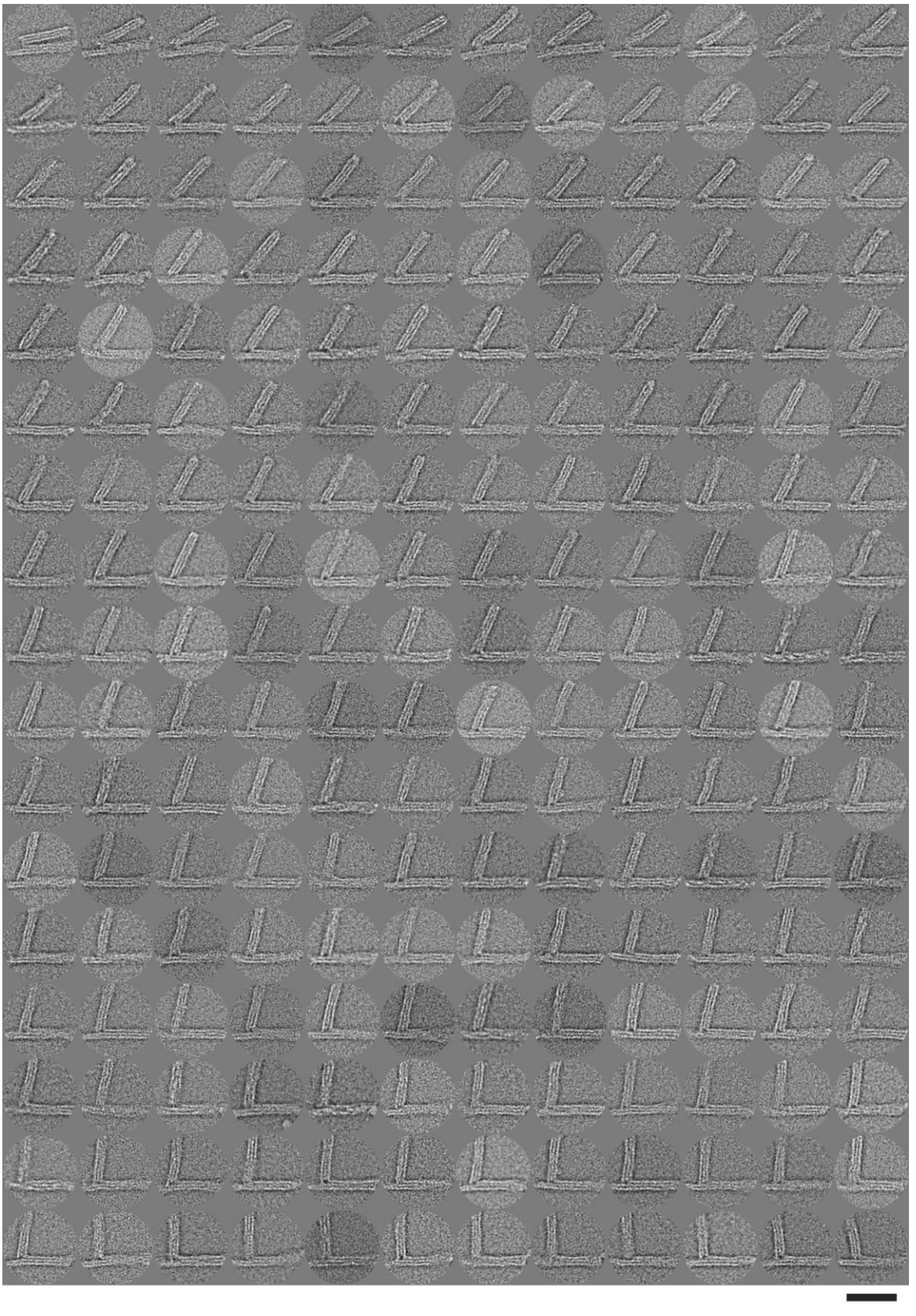

fig. S6. Exemplary particles of the force spectrometer. 210 (out of 3091) exemplary negative-stain electron micrographs of the force spectrometer without nucleosomes. Scale bar is 50 nm.

note S3. Calibration of the force spectrometer

Model for the energy landscape of the force spectrometer

The probability of measuring a particular vertex angle Θ is given by the Boltzmann-factor

$$p(\Theta)=\frac{1}{Z}e^{-\frac{E(\Theta)}{k_B T}}$$

where $p(\Theta)$ is the probability density of the vertex angle Θ, $Z=\int_0^{2\pi} e^{-E(\Theta)/k_B T}\, d\Theta$ is the partition function and $E(\Theta)$ is the energy of the force spectrometer as a function of the vertex angle.

The energy landscape of the force spectrometer can be approximated considering the properties of the hinge mechanism and electrostatic repulsion of the two arms at small vertex angles:

Hinge mechanism: Four single-stranded DNA connectors (each two bases) in parallel form the flexible hinge mechanism of the force spectrometer. In addition, four 30 bases long single-stranded DNA loops were included (fig. S5 and fig. S7). Since the persistence length of single-stranded DNA is ∼1.5 *nm* (36), we can model these loops as entropic springs with spring constants of $k=3k_BT/2PL$, where P is the persistence length and L is the contour length. Hence, the energy due to these entropic springs is

$$E_k(\Theta)=\frac{1}{2}k_{eff}\left[2a\cos\left(\frac{\Theta}{2}\right)-L_0\right]^2$$

where k_{eff} is an effective spring constant , L_0 is the mean end-to-end distance and a is the distance from the hinge to the point, where the ssDNA loops exit the force spectrometer (fig. S7).

Electrostatic repulsion of the arms: Since the backbone of DNA carries negative charges, an electrostatic repulsion between the two arms of the force spectrometer at small vertex angles is expected. We assume a constant charge density at the surface of the arms and use the Debye-Hückel approximation to compute the electrostatic energy

$$E_{DH}(\Theta)=c\int_0^{L_{arm}}\int_0^{L_{arm}}\frac{e^{-r_{q_1,q_2}/l_{debye}}}{r_{q_1,q_2}}\,dq_1 dq_2$$

where c is a constant, r_{q_1,q_2} is the distance between two point charges q_1 and q_2 on opposing arms and l_{debye}=1.6 *nm* is the debye length at the ionic strength used (10 *mM* $MgCl_2$).

We used maximum likelihood estimation (implementation from MATLAB 2015b, The MathWorks, Inc., Natick, Massachusetts, United States) to fit the model described above to the set of vertex angles (fig. S7c)

$$k_{eff}=17\pm1\ pN\,nm^{-1}$$

$$L_0 = 5.37 \pm 0.02\ nm$$

$$c = 0.02 \pm 0.01\ nm\, k_B T\, C^{-2}$$

Energy landscape and torque

The energy landscape of the force spectrometer can be obtained from the angle distributions

$$E(\Theta_i) = -\ln\left(p(\Theta_i)\right) - E_0$$

where $p(\Theta_i)$ is the kernel density estimate of probability density at location Θ_i and $E_0 = \ln(Z)$ is an unknown normalization constant (fig. S7d). Using the fit described above, we can approximate the constant

$$E_0 \approx \int_0^{2\pi/3} e^{-\beta\,(E_k(\Theta) + E_{DH}(\Theta))}\, d\Theta$$

Finally, the force spectrometer exerts a torque that can be estimated from the energy landscape: $\tau = dE(\Theta)/d\Theta$ (see fig. S7e).

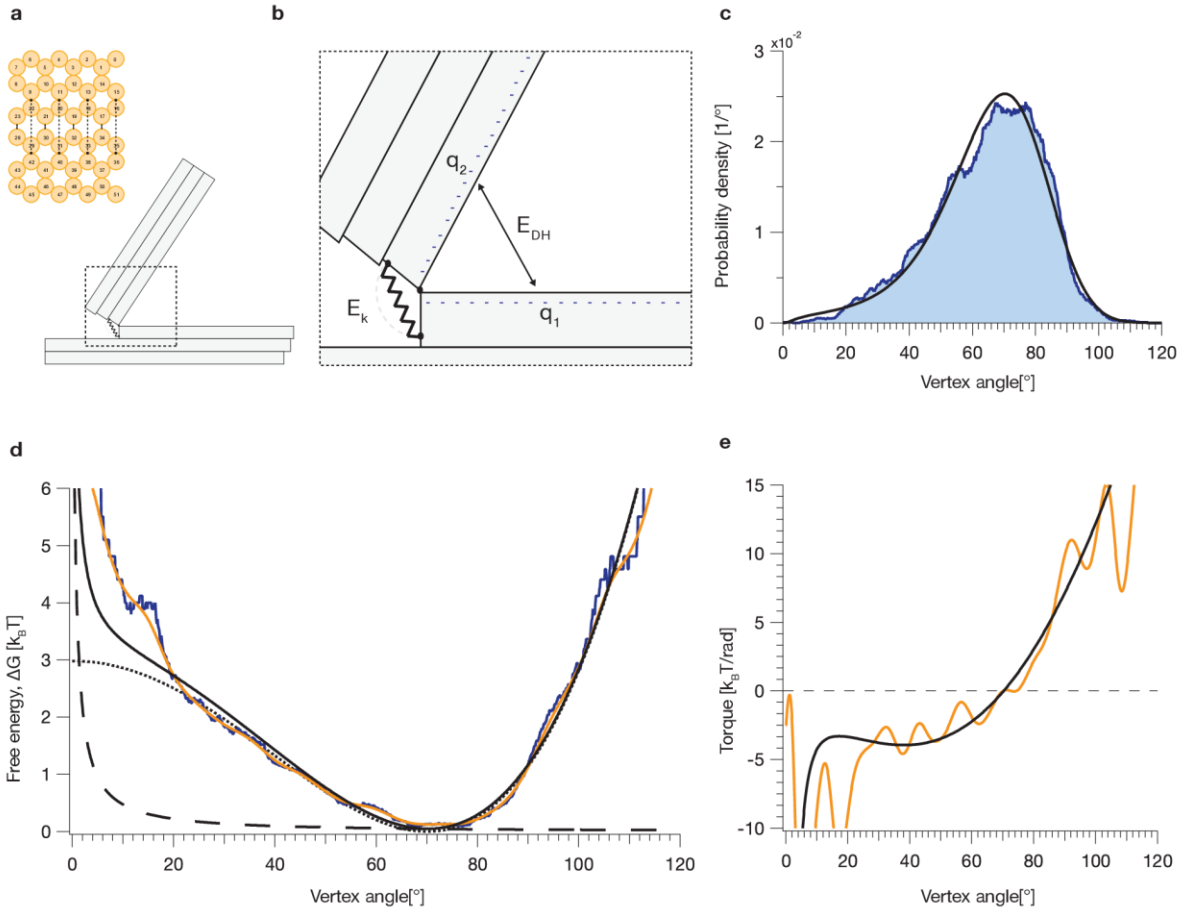

fig. S7. Characterization of the force spectrometer. (**a**) Cross section of the force spectrometer (top left), where the single-stranded DNA connections between the top arm (helix 0-23) and the bottom arm (helix 28-51) are depicted as solid lines (2 bases) and dashed lines (30 bases). Schematic of the force spectrometer (bottom right), where the section shown in b is highlighted. (**b**) Schematic model of the hinge mechanism. The 30 bases long loops are depicted as a spring with energy E_k. Surface charges (q_1,q_2 on the arms) generate an electrostatic interactions E_{DH}, that is described with the Debye-Hueckel-approximation. (**c**) Blue line: uniform kernel density estimate of the probability density of the vertex angle with bandwidth 3°. Black line: maximum-likelihood-estimation of the probability density with a model that considers the energetic contribution from the entropic springs at the hinge and the electrostatic repulsion of the two arms. (**d**) Kernel density estimates of the energy landscape of the force spectrometer with a uniform kernel (blue line) and a normal kernel (orange line) with a bandwidth of 3°. Solid black line: energy landscape of the maximum-likelihood-estimation shown in c. Black dashed line: energetic contribution of the electrostatic repulsion. Black dotted line: energetic contribution of the entropic spring potential. (**e**) Torque of the force spectrometer calculated form the normal kernel density estimation and maximum-likelihood-estimation shown in d.

note S4. Attachment of nucleosomes to the force spectrometer

Orientation of nucleosomes on force spectrometer

The nucleosomes were attached to the force spectrometer via two of the four possible single-stranded DNA attachment handles (see fig. S8a). We used attachment handle 1 and 3 since they are protruding on a similar height compared to the attachment handles 2 and 4 (fig. S8b). We expect the nucleosomes to bind such that the handles A1 and A3 are geometrically closest to the force spectrometer. This orientation was confirmed by average electron micrographs (see Fig. 4 bottom right and S13). Due to this attachment design the nucleosomes on the top with respect to the one of the bottom arm of the force spectrometer are rotated by 180° around the dyad axis and rotated around the 'cylindrical' axis (when seeing the nucleosome as a disk) perpendicular to the dyad axis since the attachment handles are not on the dyad axis. The angle between the axis going through the attachment handle positions A1 and A3 and the dyad axis is 39° (see fig. S9a). Thus, the relative angle between the top and the bottom nucleosome is 78° (see fig. S9b).

Incubation of force spectrometers with nucleosomes

Purified force spectrometers were incubated with nucleosomes of sequence sets 1 and 2 to yield a 1:3 excess of nucleosome per binding site (typically 40 nM of force spectrometer with 135 nM of nucleosome) at 4°C over night in buffer (11 mM $MgCl_2$, 5 mM TRIS base, 1 mM EDTA and 35 mM NaCl). Samples were used without further purification for the preparation of TEM grids or for gel electrophoresis experiments.

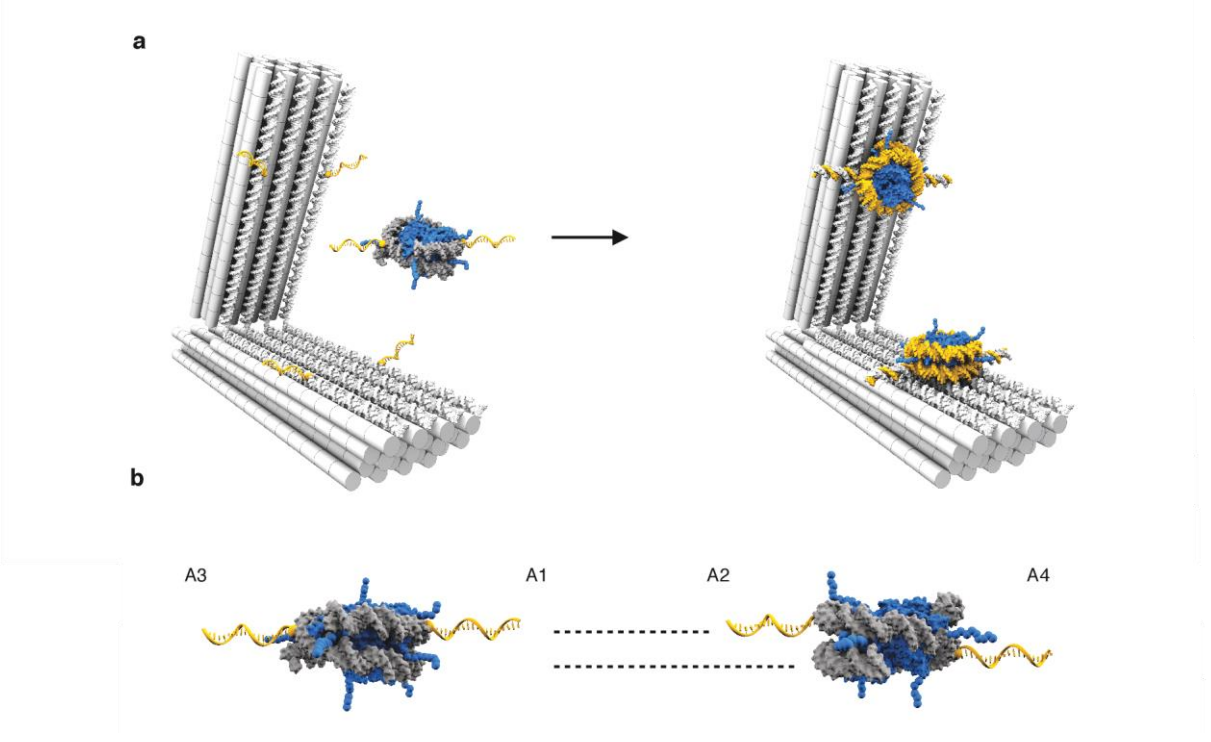

fig. S8. Attachment of nucleosomes to the force spectrometer. (**a**) Left: Schematic representation of force spectrometer with single-strand DNA (ssDNA) attachment handles at distal position and single nucleosome with complementary ssDNA handles. Right: Schematic representation of force spectrometer with two attached nucleosomes at the distal position. (**b**) Schematic representation of a nucleosome with attachment handles at position A1 and A3 (left) and at position A2 and A4 (right). Dashed lines indicate geometric 'height' of attachment handles.

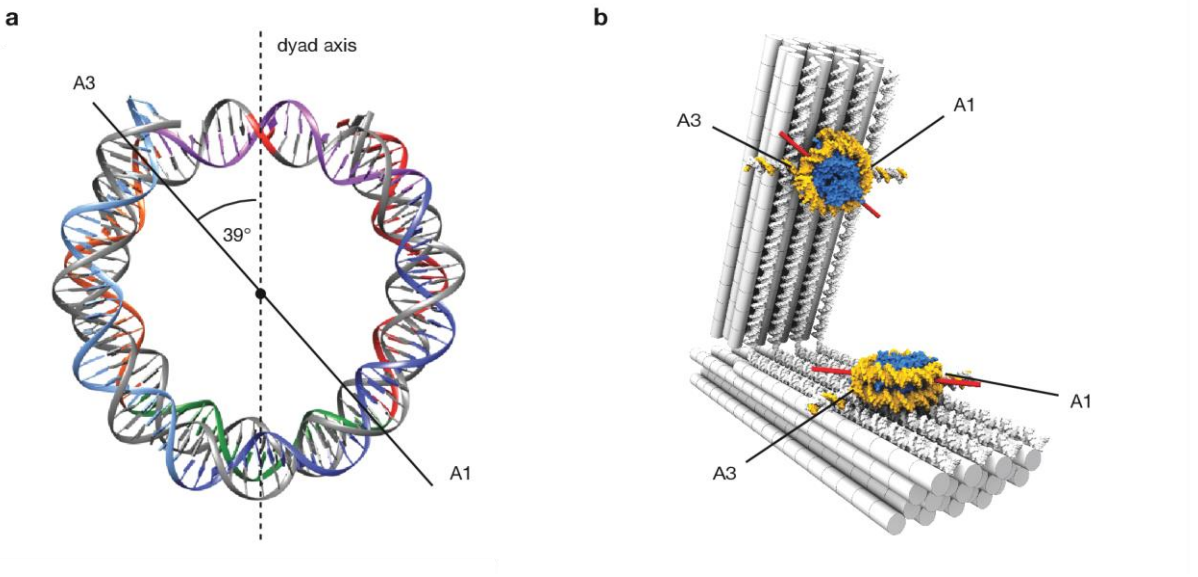

fig. S9. Orientation of nucleosomes on the force spectrometer. (**a**) Schematic view of 147 bp DNA template wrapped around the histone octamers (not shown). Individual oligos used in the template are shown in different colours. Dashed line indicates dyad axis. Solid indicate line going through attachment handle positions A1 and A3. (**b**) Schematic view of force spectrometer with two attached nucleosomes on top and bottom arm in 'distal' position. Red cylinders indicate dyad axis for each nucleosome. Attachment handle positions as indicated.

note S5. TEM imaging and particle selection

Force spectrometer samples with attached nucleosomes in 11 mM $MgCl_2$, 5 mM TRIS base, 1 mM EDTA and 35 mM NaCl were adsorbed on glow-discharged formvar-supported carbon-coated Cu400 TEM grids (Science Services, Munich, Germany) and stained using a 2% aqueous uranyl formate solution containing 25 mM sodium hydroxide. Imaging was performed using a Philips CM100 electron microscope operated at 100 kV. Images were acquired using an AMT 4 Megapixel CCD camera. Micrograph scale bars were calibrated by imaging 2D catalase crystals and using the lattice constants as a length reference. Imaging was performed at 28500-fold magnification. For image processing, libraries of individual particle micrographs were created by particle picking using the EMAN2 (62) boxing routine. Particles from all samples were subsequently randomized to avoid any bias and post-selected for particles that feature two intact bound nucleosomes at the expected positions (see fig. S11 and S12 for exemplary libraries and fig. S10 for particle-selection rules). Vertex angles of selected single particles were measured using ImageJ (1.49v) (63). Generation of average particle micrographs was performed using Xmipp mlf_2Dalign routine (64) and IMAGIC (Image Science Software GmbH, Berlin, Germany).

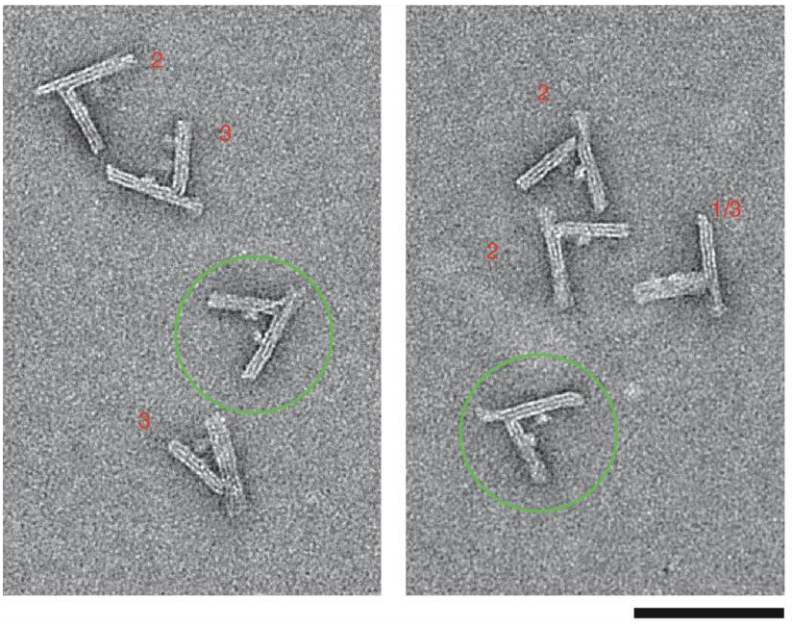

fig. S10. Rules for particle selection. Two exemplary field-of-views of force spectrometers incubate with nucleosomes with wildtype histones. Particles labelled with a green circle were selected as good particles. The other particles were neglected due to the following reasons (indicated by red number): 1: No nucleosome bound, 2: Only one nucleosome bound, 3: Force spectrometer or at least one nucleosome distorted, presumably due to surface interactions.

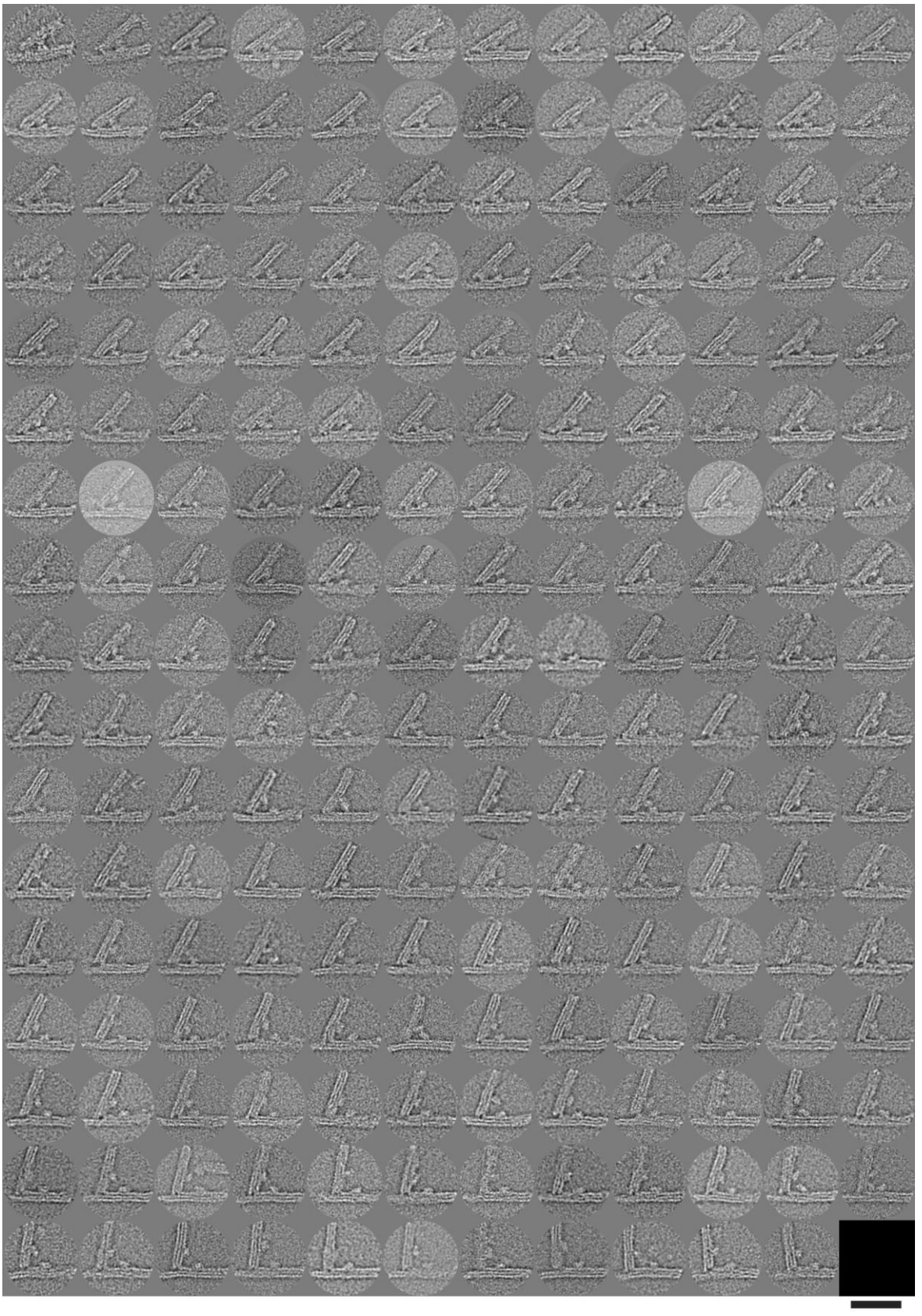

fig. S11. Exemplary particles of the force spectrometer with two bound NCPs (wild-type and *X. laevis*) at the proximal position. 203 (out of 1301) exemplary negative-stain electron micrographs of the force spectrometer with two bound nucleosomes in the proximal position with wildtype histones. Scale bar is 50 nm.

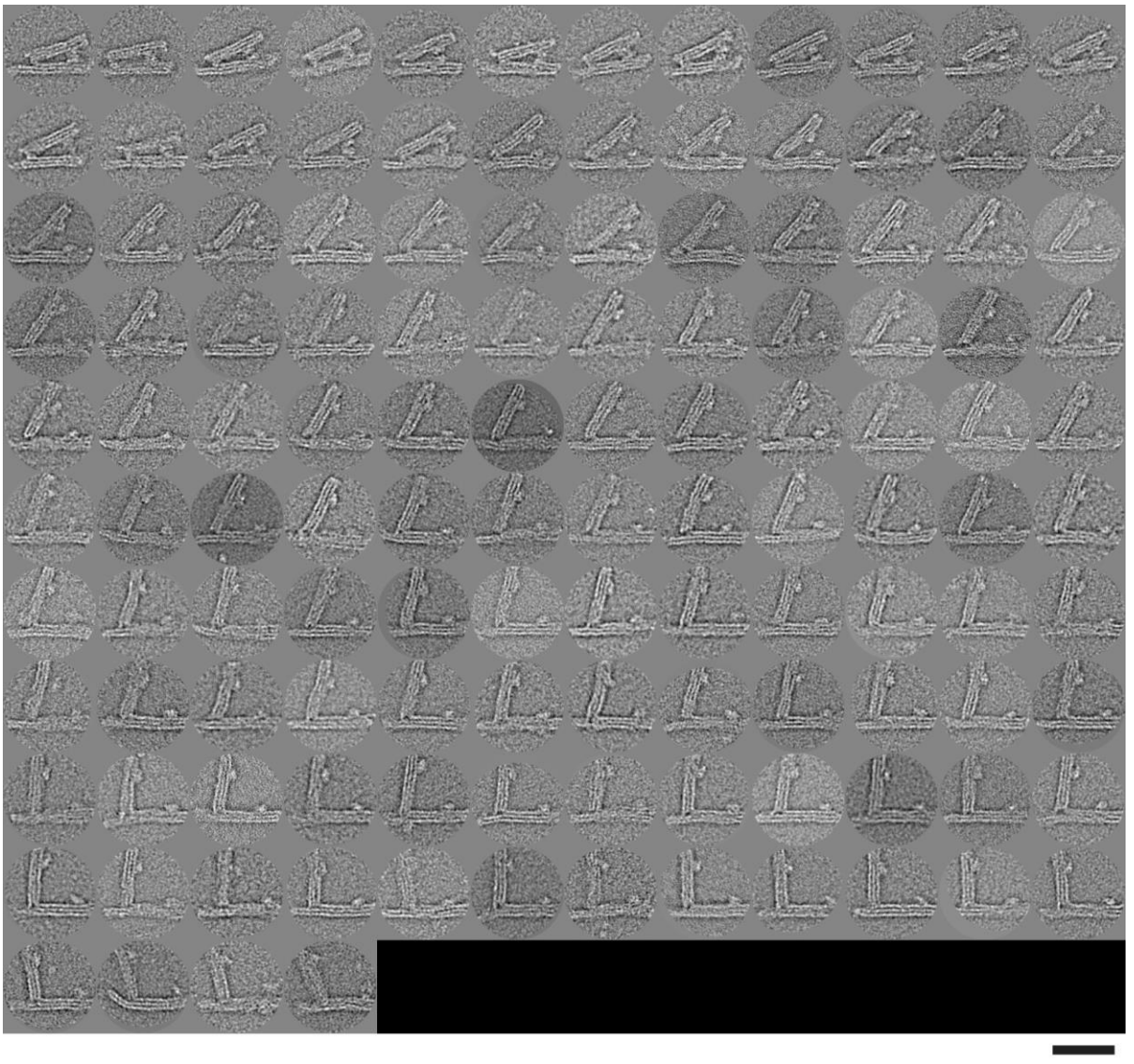

fig. S12. Exemplary particles of the force spectrometer with two bound NCPs (wild-type and *X. laevis*) at the distal position. 124 (out of 158) exemplary negative-stain electron micrographs of the force spectrometer with two bound nucleosomes at the distal position. Scale bar is 50 nm.

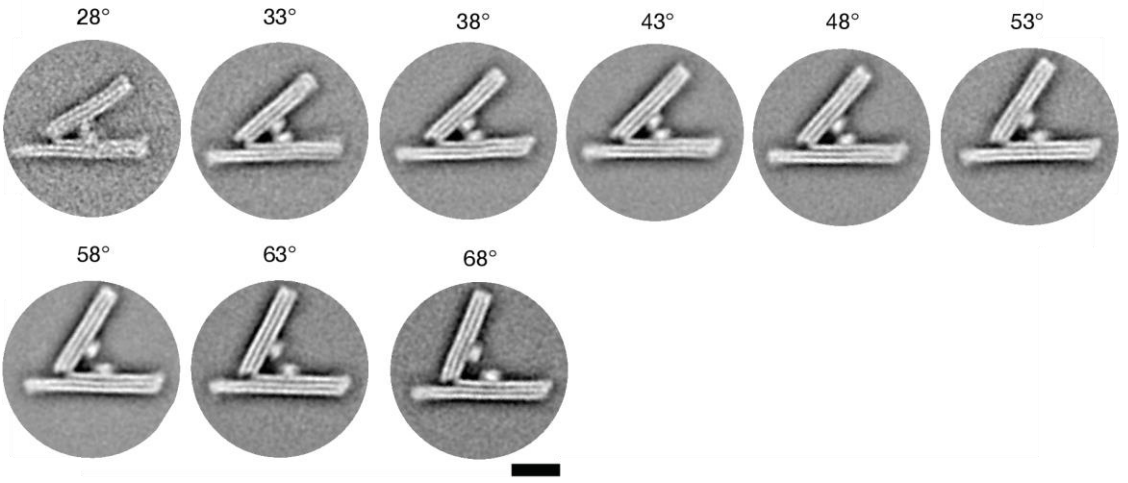

fig. S13. Average micrographs of force spectrometers with attached NCPs (wild-type and *X. laevis*) at the proximal position. Average negative-staining micrographs of force spectrometers with two bound wildtype nucleosomes (*Xenopus laevis*) at the proximal position. For each average only particles with a vertex angle that fell in a 5°-window around the indicated value were considered. Scale bar is 25 nm.

note S6. Comparison of negative staining versus cryo-EM

Electron cryo microscopy

Samples of force spectrometers with or without attached nucleosomes (in 11 mM $MgCl_2$, 5 mM TRIS base, 1 mM EDTA and 35 mM NaCl) were incubated for 120 *s* on glow-discharged lacey carbon grids with ultrathin carbon film (TED PELLA, 01824) and vitrified using a freeze-plunging device (Vitrobot Mark IV, FEI). Samples were imaged at liquid nitrogen temperatures using a Tecnai Spirit TEM (FEI) operated at 120 kV with a 4x4k Eagle CCD Detector (FEI) at 26000x (pixel size 4.188 Å) or 30000x (pixel size 3.574 Å) magnification with a defocus of -2 μ*m* to -1 μ*m*.

Comparison of negative staining versus cryo-EM

Typical field-of-view micrographs obtained using negative staining and under cryogenic conditions are given in fig. S14. The appearance of bare spectrometer particles in negative staining versus cryogenic EM micrographs were very similar (fig. S14A left versus right). Under both conditions the particles sample a distribution of opening angles. However, the appearance of spectrometer particles that were functionalized with nucleosomes differed in that the transmission contrast produced by the nucleosomes is lower in cryo-EM as opposed to negative staining (fig. S14B right versus left). In negative staining, classifying the particles according to whether they feature correctly attached nucleosomes is straightforward (green check marks versus red crosses in fig. S14B left). By contrast, sorting the particles from cryo-EM is more challenging (white arrows in fig. S14B right). In particular, due to the reduced contrast it is difficult to discriminate between particles having two nucleosomes in the desired configuration where the disc is parallel to the spectrometer beam surfaces versus particles having one or two nucleosomes with incomplete attachment.
We have analyzed our cryo-EM data sets in greater detail. We find that the bare spectrometer particles as seen in cryo-EM sample the full range of opening angles in the same way as in negative staining (fig. S15A). The detailed appearance of particles (three stripes along the beams, hinge region) is very similar besides positive contrast in cryo-EM versus negative contrast in the uranyl-formate stained samples. Cryo-EM particles functionalized with two nucleosomes also sample the full range of opening angles as the negative stained particles (fig. S15B). In particular, there are again particles with two nucleosomes in close contact as well as particles in which the nucleosomes are far apart. We analyzed the opening angles for bare spectrometer particles and particles functionalized with wild type nucleosomes from *Xenopus laevis* as seen in cryo-EM. The angle distributions (fig. S16A) and energy landscapes (fig. S16B) obtained from cryo-EM versus negative staining compare well, with the caveat that the cryo-EM distributions for particles with nucleosomes may contain more data points from falsely classified particles. Importantly, the differential nucleosome-nucleosome interaction energy landscape obtained from cryo-EM (fig. S16C) reflects the same features as the one obtained from negative staining: strong repulsion at short distances, a minimum of - 1.4 kcal/mol at 6 nm, and a long range. Interestingly, we observe that the distribution of opening angles for the bare spectrometer as seen in cryo-EM is a bit narrower than the one seen in negative staining; fewer particles have small opening angles in cryo-EM as compared to negative staining conditions (fig. S16A). However, the distribution of opening angles seen for particles with two nucleosomes as seen in cryo-EM also has now fewer particles with small opening angles. Fewer particles populating small angles as seen for both the bare spectrometer and also the spectrometer with nucleosomes may mean that the energetic penalty for closing the spectrometer is slightly higher in the cryo-EM conditions. Since our method relies on a differential comparison of data with and without nucleosomes, the resulting nucleosome-nucleosome energy landscape is not affected.

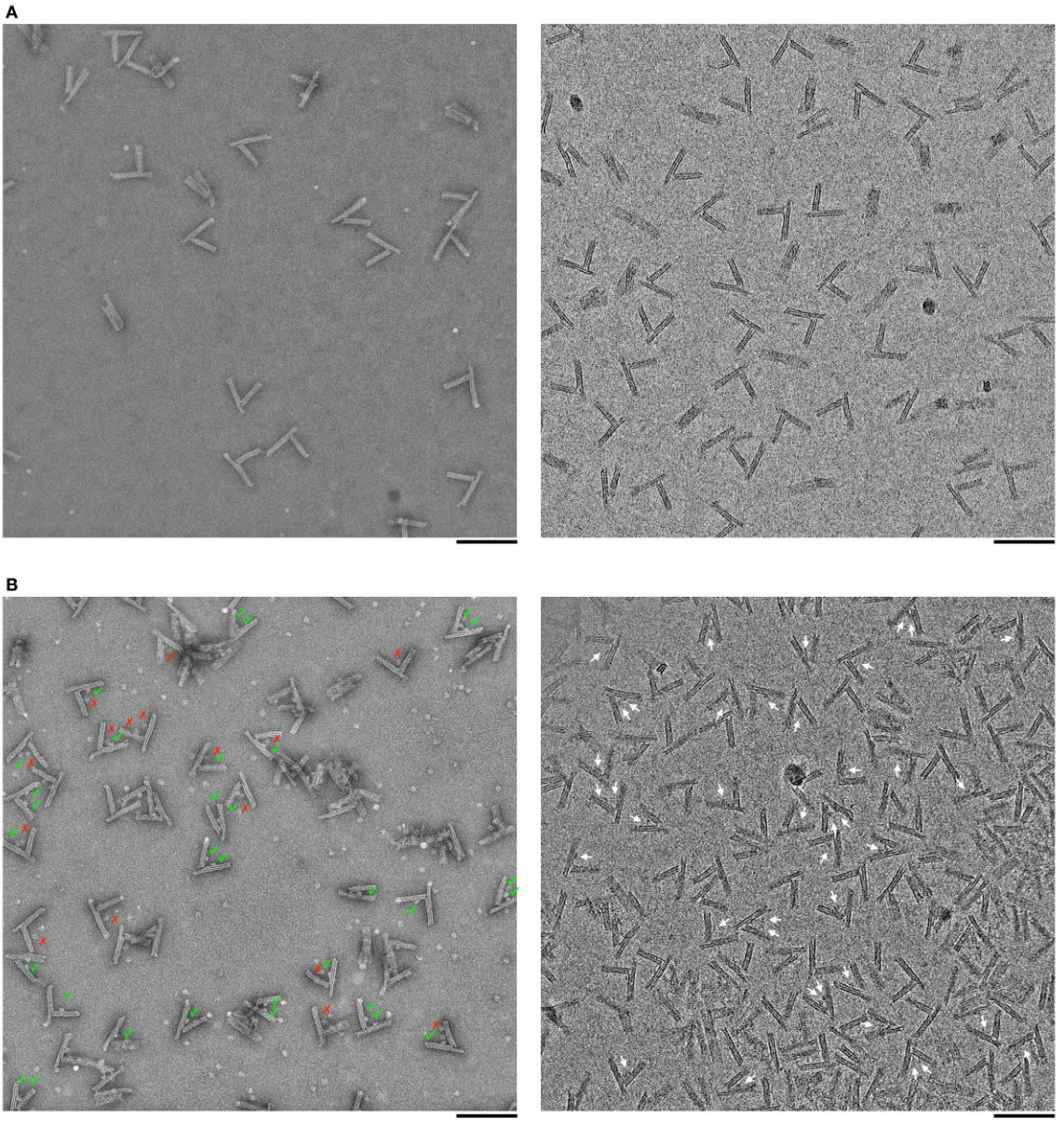

fig. S14. Negative staining versus cryo-EM micrographs. (**A**) Field-of view micrographs with bare spectrometer particles. Left: negative staining. Right: in vitrified ice. (**B**) Typical micrographs of spectrometer particles with nucleosomes at the proximal position containing wild type *Xenopus laevis* histones. Left: negative staining. Green check marks vs red crosses indicate correctly or incorrectly attached nucleosomes, respectively. Right: in vitrified ice. The sample is 1:2 mixture of bare spectrometer particles with nucleosome-functionalized particles. White arrows indicate particles with nucleosome density. Micrographs were high-pass filtered removing frequencies below ~1/(50 *nm*). Scale bars: 100 nm.

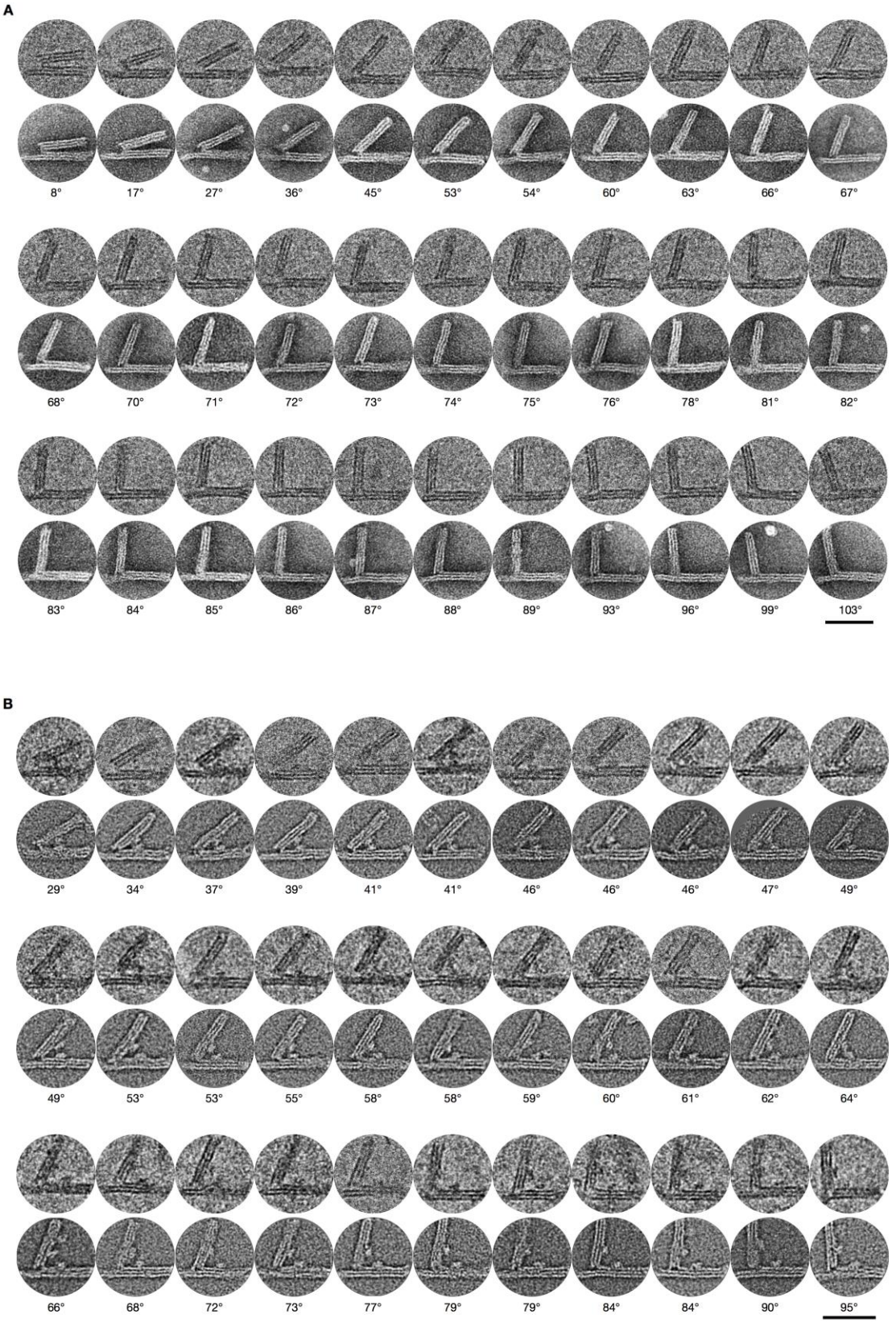

fig. S15. Comparison of single particles from negative staining versus cryo-EM. Exemplary single-particle micrographs, obtained from (**A**) the bare spectrometer and (**B**) from spectrometers functionalized with two wild type *Xenopus laevis* nucleosomes at the proximal attachment position. Top rows: cryo-EM. Bottom rows: negative staining. Numbers give opening angles. Scale bars: 50 nm.

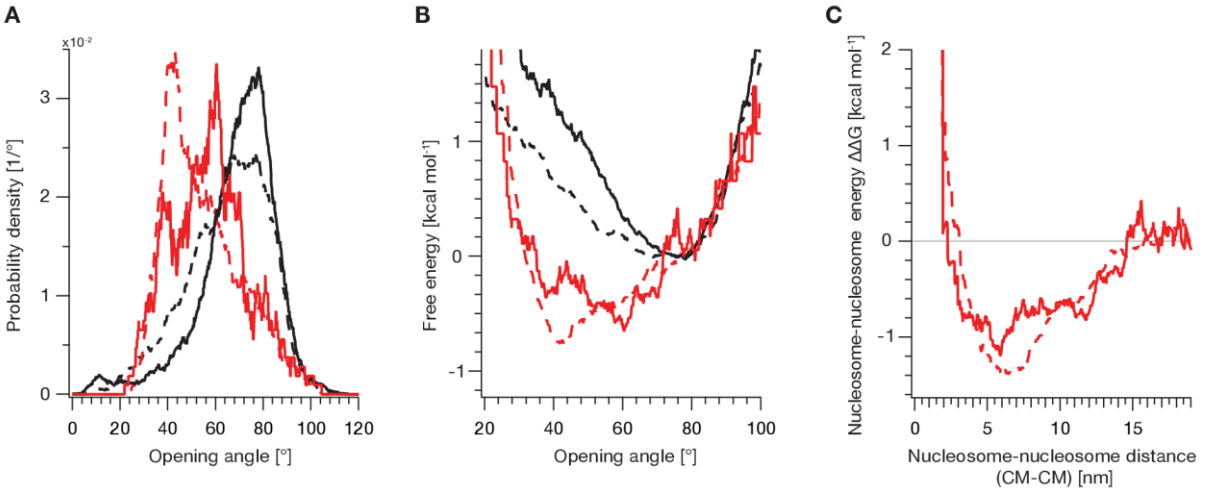

fig. S16. Quantitative comparison of distributions and energy landscapes from negative staining versus cryo-EM. Uniform kernel density estimates (bandwith 3°) for (**A**) opening angle distributions and (**B**) energy landscapes of single spectrometer particles. Solid lines: cryo-EM. Dashed lines: negative staining. Black lines: bare spectrometer. Red lines: spectrometer with two nucleosomes at the proximal position containing wild type *Xenopus laevis* histones. (**C**) Nucleosome-nucleosome free energy landscape obtained from negative staining data (dashed line) and cryo-EM data (solid line).

note S7. Gel-based measurements of ensemble FRET

Gel electrophoresis and image acquisition

Samples were electrophoresed for 2 h and 30 min at 70 *V* on ice cooled 2% agarose gels, where both gel buffer and running buffer contained 0.5 TBE (1 mM EDTA, 44.5 mM Tris base, 44.5 mM boric acid, pH ~ 8.3) and 11 mM $MgCl_2$. Gels were laser scanned using a Typhoon Fla 9500 (GE Healthcare) with a resolution of 50 µ*m*/*pixel* in three channels:

Channel	Excitation [nm]	Emission window [nm]
$A_{em}\|D_{ex}$	532	≤ 665
$D_{em}\|D_{ex}$	532	560-580
$A_{em}\|A_{ex}$	635	≤ 665

The calculation of FRET efficiencies and depiction of laser scanned agarose gels follows the scheme shown in fig. S17.

Correction of laser-scanned images

Laser-scanned images were corrected and analyzed according to (32). In brief, the analysis followed two steps:

Background correction: The background fluorescence of each channel was estimated by using the mean fluorescence intensity of four manually selected areas, where no sample was present. A two-dimensional second order polynomial was fitted to these mean intensities and subtracted from the original image.

Correction for direct excitation and leakage: Significant cross-talk was observed only for the *Aem|Dex*-channel, which is due to direct excitation of the acceptor molecule and leakage of the donor fluorescence into the acceptor detection window. A sample containing only an acceptor molecule and a sample containing only a donor molecule were included in each gel and used to calculate two correction factors: β_{leak} and β_{dir}. β_{dir} was calculated from the slope of a scatter-plot where the intensity of each pixel in the monomer band of channel *Aem|Dex* was plotted against the intensity of channel *Aem|Aex*. The correction factor β_{leak} can be calculated accordingly by plotting for each pixel the intensity of channel *Aem|Dex* against the intensity in channel *Dem|Dex*. Finally, for each pixel the corrected intensity can be calculated as

$$I_{D|A}^{cor} = I_{D|A}^{bg} - \beta_{leak} I_{D|D}^{bg} - \beta_{dir} I_{A|A}^{bg}$$

where I^{bg} is the background-corrected intensity of the given channel.

Calculation of FRET efficiencies

The gel-based assay enables the comparison between the FRET efficiencies of monomer bands from multiple samples in parallel.

Pixel-level depiction of FRET images

The FRET efficiency of a given pixel (*i*,*j*) can be calculated from the ratio of fluorescence intensity in the *Dem|Dex*-channel and the fluorescence intensity in the *Aem|Dex*-channel

$$E_{\{i,j\}} = \left(1 + \gamma \frac{I_{D|D,\{i,j\}}}{I_{A|D,\{i,j\}}}\right)^{-1}$$

where γ is a factor that depends on the detection efficiencies of the channels and quantum yields of the donor and acceptor molecule. We determined this factor for each gel individually using a reference sample with defined FRET efficiency of 0.5. The factor was typically around $\gamma \approx 1.1$ (fig. S18). In the regions of the images where no sample is present, small variation in the background fluorescence can lead to large variations in the FRET efficiency for the background signal. We therefore applied an opacity mask *O* that is computed as follows

$$E_{\{i,j\}} = \min\left(\frac{I_{A|A,\{i,j\}}}{c}\right)$$

where *c* is a normalization constant above which the opacity is one. We chose *c*=5000, since monomer bands showed fluorescence intensities above ~5000, while the background fluorescence was on the order of 10−100 counts.

Quantitative comparison of FRET efficiencies

Assuming a single population for a given monomer band, we can calculate the FRET efficiency of this band as follows

$$E_{band} = (1+\gamma\, r)^{-1}$$

where *r* is the mean ratio between the *Dem|Dex*-channel and the *Aem|Dex*-channel. It is determined by plotting for each pixel in a selected area the fluorescence intensities of the *Dem|Dex*-channel against the fluorescence intensity of the *Aem|Dex*-channel and fitting a linear relation to this scatterplot, since $I_{D|D} \propto I_{D|A}$ (fig. S18 and S19).

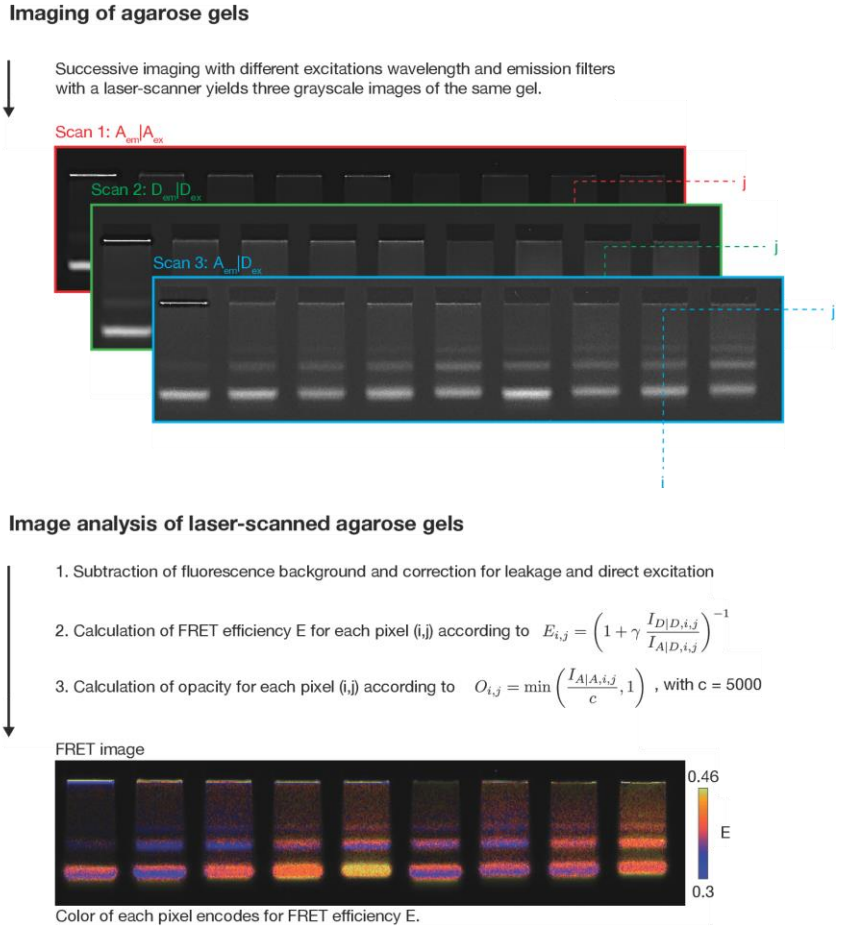

fig. S17. Calculation of FRET efficiencies and depiction of laser-scanned agarose gels. Detailed description of each step is given in the text.

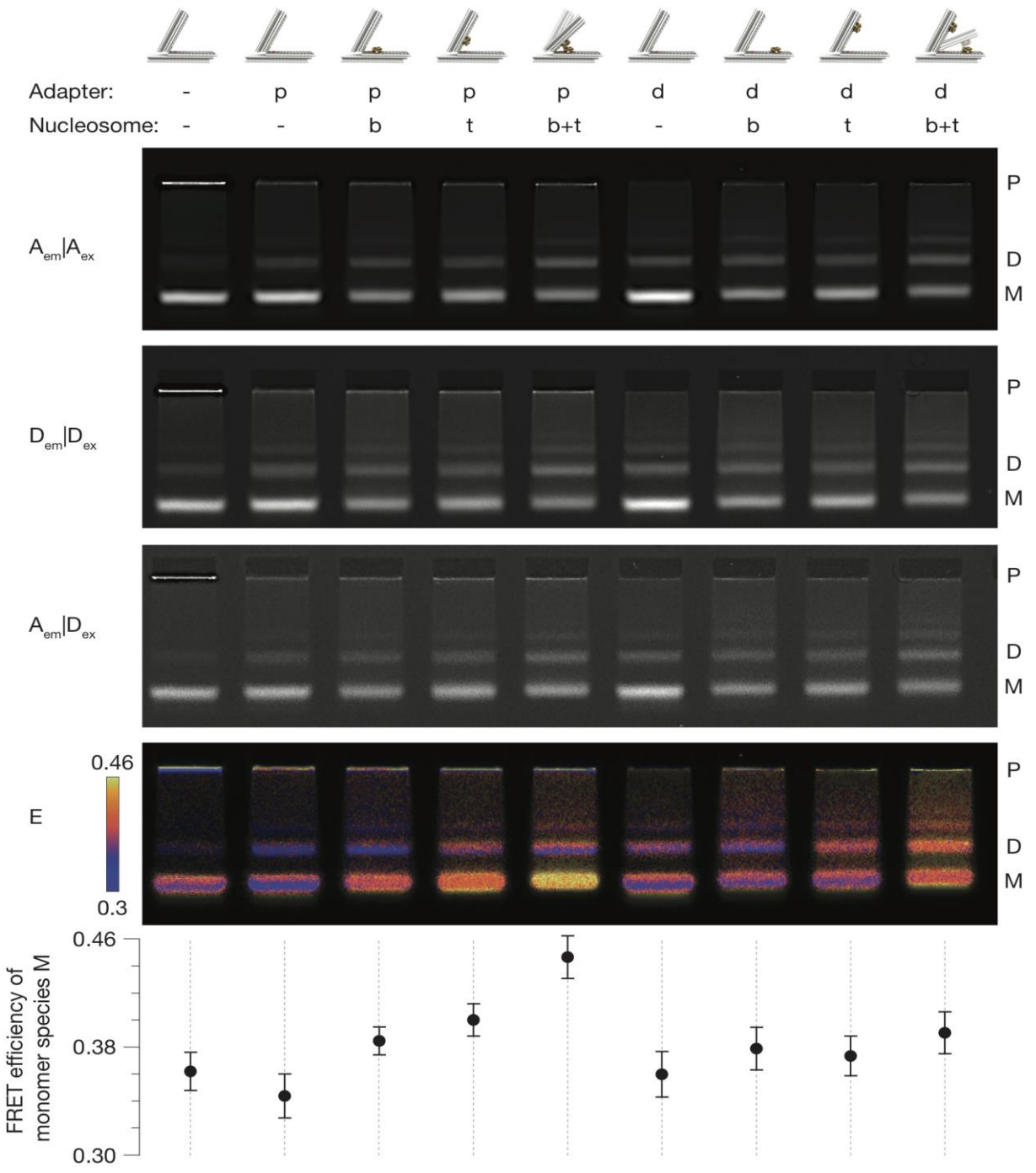

fig. S18. Nucleosome-nucleosome interaction observed using gel-based ensemble FRET measurements. Images of laser-scanned gels in three channels (*Aem|Aex*, *Dem|Dex* and *Aem|Dex*) on which samples of force spectrometers ("-": without nucleosome-adapters, p: nucleosome-adapters protrude at proximal positions, d: nucleosome-adapters protrude at distal positions), which were previously incubated with nucleosomes ("-": incubation without nucleosomes, b/t: incubation with nucleosomes that have ssDNA handles that are complementary to the nucleosome-adapter protruding from the bottom arm (b) or top arm (t)) were electrophoresed. Pocket (P), dimer band (D) and monomer band (M) are indicated. E: FRET efficiency calculated for each pixel. An opacity mask was applied to highlight areas where sample is present. Bottom row: FRET efficiency calculated for each monomer band.

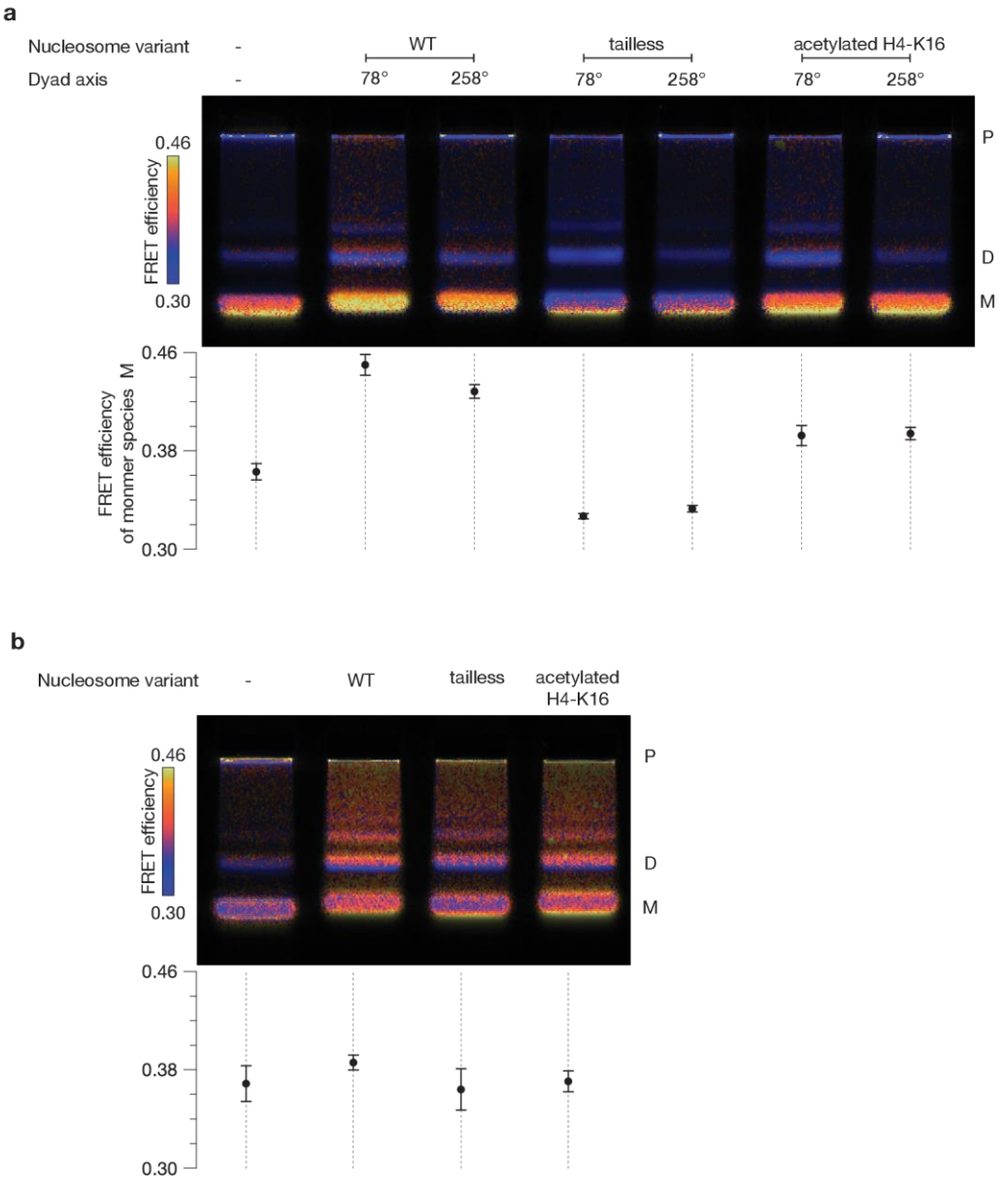

fig. S19. Gel-based ensemble FRET measurements of nucleosome variants and orientations. FRET efficiency images calculated for each pixel from laser scanned images of gels on which samples of force spectrometers with attached nucleosomes where electrophoresed. Force spectrometer samples were incubated with different nucleosome variants and in different orientations. (**a**) Nucleosome-adapters protrude at proximal positions. Two relative nucleosome-orientations where implemented by interchanging the protruding sequences from the bottom arm that are described by the angle between their nucleosomes dyad axis (**b**) Nucleosome-adapters protrude at distal positions and the dyad axis intersect at an angle of 78°.

note S8. Calculation of nucleosome-nucleosome energy landscapes

In order to extract the energy landscape of two nucleosomes from the set of measured vertex angles, we first estimate the probability density $p(\Theta)$ of each variant using kernel density estimation with a uniform or normal kernel and a bandwith of 3°. Assuming Boltzmann statistics, the probability density is given by

$$p(\Theta)=\frac{1}{Z}e^{-\frac{E(\Theta)}{k_BT}}$$

with the partition function $Z=\int_0^{2\pi} e^{-E(\Theta)/kBT}d\Theta$. Hence, the free energy landscape of a given sample can be calculated (fig. S20, a and b)

$$\frac{E(\Theta)}{kBT} = -\ln(p(\Theta))-\ln(Z)$$

where $\ln(Z)$ is a constant that depends on the underlying energy landscape, i.e. the nucleosome-variant. In order to compare different samples, we assume that the interaction between nucleosomes vanishes at large distances. We can therefore shift each energy landscape by a variant-dependent constant Δ_i

$$\frac{E_i(\Theta)}{k_BT} = -\ln(p_i(\Theta))+\Delta_i \qquad (1)$$

$$with\ \Delta_i = \ln\left(\frac{\int_{\Theta_0}^{2\pi} p_i(\Theta)\,d\Theta}{\int_{\Theta_0}^{2\pi} p_{noNCP}(\Theta)\,d\Theta}\right)$$

where *pnoNCP* is the density estimate of the bare spectrometer and $\Theta 0=75^\circ$ (≈15.4 nm CM-CM distance) is a cut off at which the interaction vanishes (fig. S20 c, d). The integrals were approximated by sums over the kernel density estimates of the probability densities with an upper integration limit of 120°.

The pair-potential of two nucleosomes can then be calculated

$$E_{i,NCP-NCP}(\Theta) = E_i(\Theta))-E_{noNCP}(\Theta)$$

$$= k_BT\ [-\ln(p_i(\Theta))+\Delta_i+\ln(p_{noNCP}(\Theta))]$$

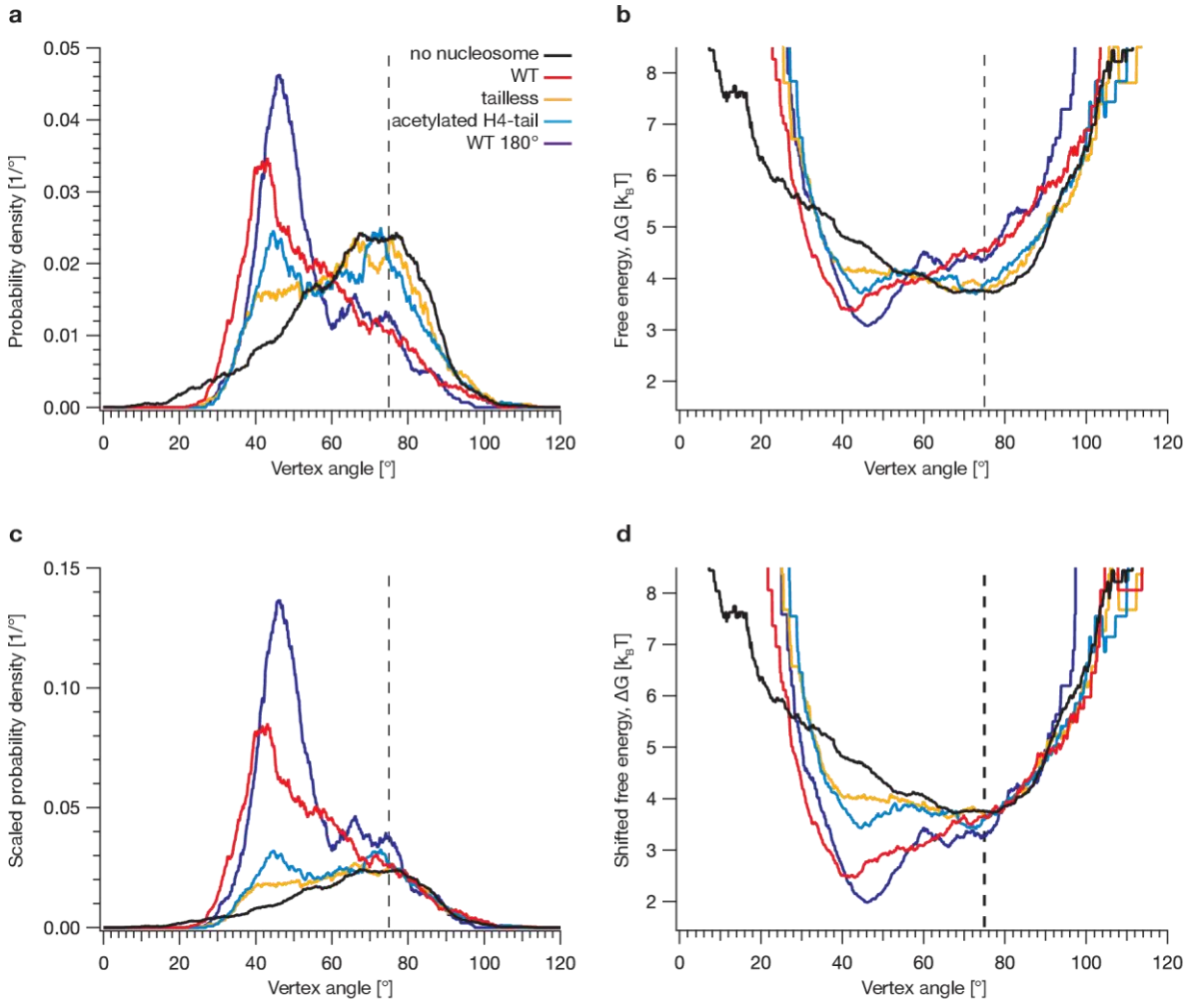

fig. S20. Calculation of free-energy landscapes. (**a**) Uniform kernel density estimates $p_i(\Theta)$ (bandwith 3°) of probability densities for constructs with different nucleosome variants and nucleosome orientations. (**b**) Free energy computed as $\Delta G = -\ln(p_i(\Theta))$. (**c**) Scaled uniform kernel density estimates $p'_i(\Theta) = p_i(\Theta)\, e^{-\Delta i}$, where the offset Δi was calculated according to eq. (1) with a cut off at 75° (dashed line). (**d**) Shifted energy landscapes $\Delta G = -\ln(p_i(\Theta)) + \Delta i$.

note S9. Geometric nucleosome arrangement on the force spectrometer

The force spectrometer constrains the geometry in which the nucleosomes interact. We therefore build a three dimensional model using *3MVD.pdb* and assuming the backbone positions where the single-stranded DNA handles protrude as points that are fixed in space by the spectrometer (fig. S21a). We used this model to compute the distance between the centers-of-mass (CM) of the nucleosomes as a function of vertex angle (fig. S21b). In addition, we found that the two nucleosome orientations used in this work have steric clashes at different CM-CM distances. This can be seen by considering the closest distance between two residues on opposing nucleosomes (fig. S21c).

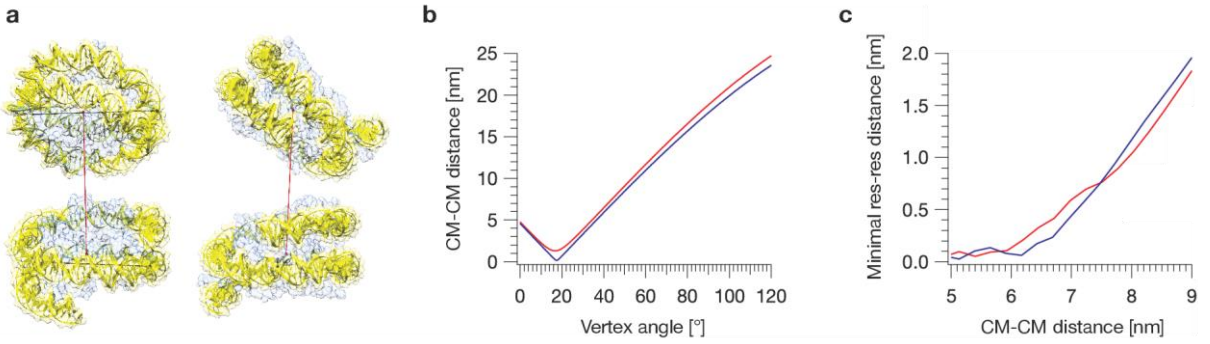

fig. S21. Configuration of nucleosomes on the force spectrometer. (**a**) To views of an assumed configuration of nucleosomes in a force spectrometer (based on 3MVD.pdb) with an vertex angle of 50°. Black handles: axis on which the nucleosomes are anchored via the attachment handles (not shown). Red spheres: location of center-of-mass (CM) position. Red line: CM-CM distance. (**b**) CM-CM distance as a function of vertex angle for a nucleosome configuration in which the dyad axis intersect at 78° (red line, configuration shown in a) and 258°. (**c**) Closest distance between residues on the top and bottom arm as a function of CM-CM distance for a nucleosome configuration in which the dyad axis intersect at 78° (red line, configuration shown in a) and 258°.

note S10. Gay-Berne potentials fitted to energy landscapes

We fitted the energy landscapes (as shown in Fig. 4) with Gay-Berne-potentials that were used previously for modelling nucleosome-nucleosome interactions (42). We used the Gay-Berne potential (41) written as follows

$$V(x)=4e\left(\left(\frac{s_0}{x-x_0+s_0}\right)^{12}-\left(\frac{s_0}{x-x_0+s_0}\right)^{6}\right)$$

The fits were performed between CM-CM distances of 3.15 and 18.8 nm The resulting curves are shown in fig. S22. The obtained fit parameters are:

Variant	$e[k_BT]$	$s_0[nm]$	$x_0[nm]$
Nucleosomes lacking N-terminal tails	0.59±0.03	16.14±0.65	4.23±0.04
WT nucleosomes where dyad axis enclose an angle of 78°	2.29±0.05	17.43±0.48	3.24±0.04
Nucleosomes where the lysine 16 at the H4-Tail is acetylated	0.93±0.03	16.65±0.48	4.25±0.03
WT nucleosomes where dyad axis enclose an angle of 258°	2.16±0.06	20.21±0.68	3.07±0.04

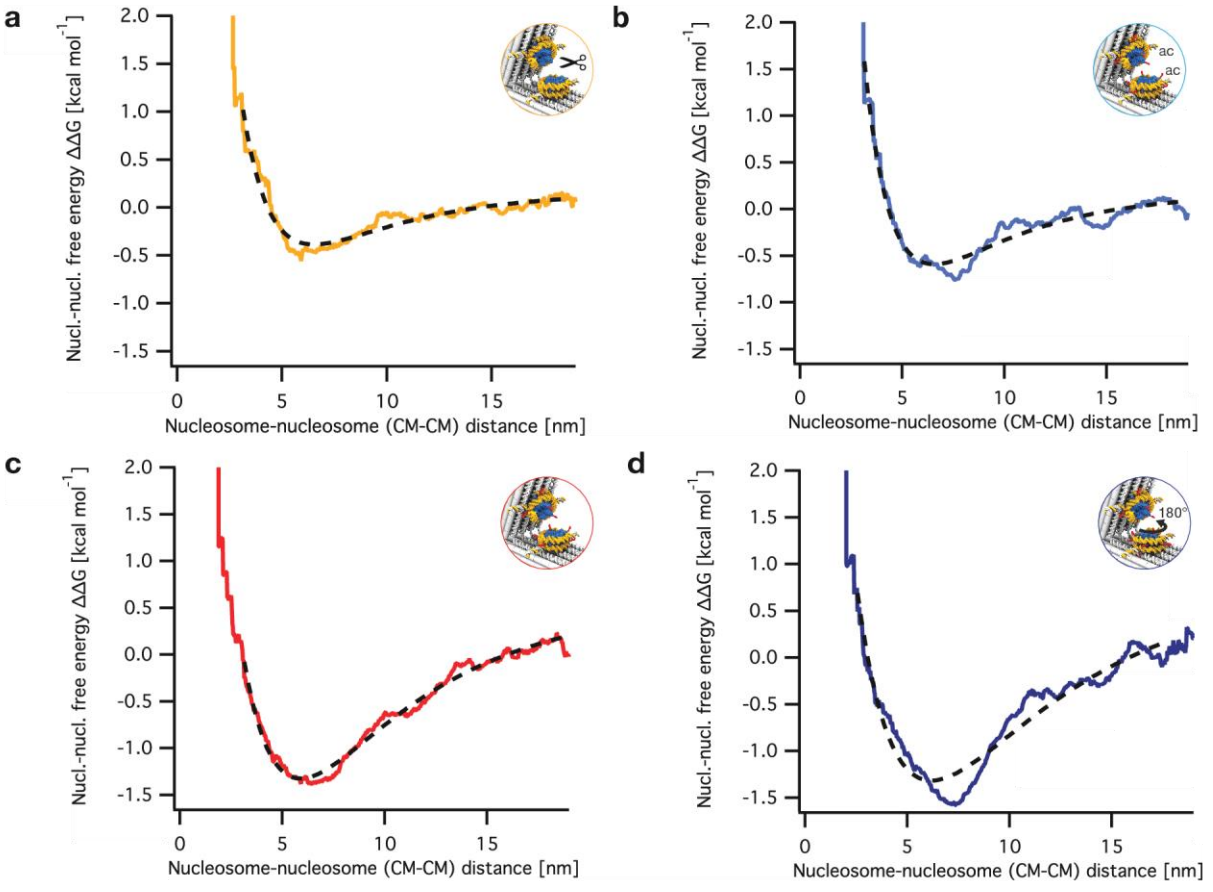

fig. S22. Gay-Berne potential fits. Fits (dashed lines) of Gay-Berne potentials to pair-potentials of nucleosomes lacking N-terminal tails (**a**) nucleosomes, where the lysine 16 at the H4-tail is acetylated (**b**) WT nucleosomes, where the dyad axis enclose an angle of 78° (**c**) and WT nucleosomes, where the dyad axis enclose an angle of 256° (**d**).